

Title	Large piezoelectric response and ferroelectricity in Li and V/Nb/Ta co-doped w-AlN
Authors	Noor-A-Alam, Mohammad;Olszewski, Oskar Zbigniew;Campanella, Humberto;Nolan, Michael
Publication date	2020-12-31
Original Citation	Noor-A-Alam, M., Olszewski, O. Z., Campanella, H. and Nolan, M. (2021) 'Large Piezoelectric Response and Ferroelectricity in Li and V/Nb/Ta Co-Doped w-AlN', ACS Applied Materials & Interfaces, 13(1), pp. 944-954. doi: 10.1021/acsami.0c19620
Type of publication	Article (peer-reviewed)
Link to publisher's version	https://pubs.acs.org/doi/10.1021/acsami.0c19620 - 10.1021/acsami.0c19620
Rights	© 2020 American Chemical Society. This document is the Accepted Manuscript version of a Published Work that appeared in final form in ACS Applied Materials and Interfaces, copyright © American Chemical Society after peer review and technical editing by the publisher. To access the final edited and published work see https://pubs.acs.org/doi/10.1021/acsami.0c19620
Download date	2024-11-09 03:19:18
Item downloaded from	https://hdl.handle.net/10468/11283



UCC

University College Cork, Ireland
Coláiste na hOllscoile Corcaigh

Large Piezoelectric Response and Ferroelectricity in Li and V/Nb/Ta co-doped w -AlN

Mohammad Noor-A-Alam^{1*}, Oskar Z. Olszewski¹, Humberto Campanella¹, and Michael Nolan^{1,2*}

1. Tyndall National Institute, Lee Maltings, Dyke Parade, University College Cork, Cork, T12 R5CP, Ireland

2. NIBEC, School of Engineering, Ulster University, Shore Road, Antrim, Northern Ireland

**Corresponding author: Mohammad Noor-A-Alam (mda.alam@tyndall.ie) and Michael Nolan (michael.nolan@tyndall.ie)*

E-mail: mda.alam@tyndall.ie;michael.nolan@tyndall.ie

Abstract

Enhancement of piezoelectricity in w -AlN is desired for many devices including resonators for next generation wireless communication systems, sensors, and vibrational energy harvesters. Based on density functional theory, we show that Li and X (X=V, Nb and Ta) co-doping in 1Li:1X ratio transforms brittle w -AlN crystal to ductile, along with broadening the compositional freedom for significantly enhanced piezoelectric response, promising them to be good alternatives of expensive Sc. Interestingly, these co-doped w -AlN also show quite large spontaneous electric polarization (e.g., about 1 C/m² for Li_{0.125}X_{0.125}Al_{0.75}N) with the possibility of ferroelectric polarization switching, opening new possibilities in wurtzite nitrides. Increase in piezoelectric stress constant (e_{33}) with

decrease in elastic constant (C_{33}) results enhancement in piezoelectric strain constant (d_{33}), which is desired for improving the performance of bulk acoustic wave (BAW) resonators for high frequency RF signals. Also, these co-doped w -AlN are potential lead-free piezoelectric materials for energy harvesting and sensors as they improves the longitudinal electromechanical coupling constant (K_{33}^2), transverse piezoelectric strain constant (d_{31}), and figure of merit (FOM) for power generation. However, the enhancement in K_{33}^2 is not as pronounced as that in d_{33} , because co-doping increases dielectric constant. The longitudinal acoustic wave velocity (7.09 km/s) of $\text{Li}_{0.1875}\text{Ta}_{0.1875}\text{Al}_{0.625}\text{N}$ is quite comparable with that of commercially used piezoelectric LiNbO_3 or LiTaO_3 in special cuts (about 5~7 km/s) despite the fact that the acoustic wave velocities, important parameters for designing resonators or sensors, drop with co-doping or Sc concentration.

Keywords: DFT, Piezoelectricity, Ferroelectricity, w -AlN, Nitrides, Doping.

Introduction

Aluminum Nitride in the wurtzite crystal structure (w -AlN) is an excellent piezoelectric material for resonators such as thin-film bulk acoustic resonators (FBARs) and solidly mounted resonators (SMRs), which are promising for radio frequency (RF) filters for telecommunication systems that operate at over 5 GHz¹⁻⁶. The key advantages of w -AlN are its high Curie temperature of 1150°C, high acoustic velocity, high quality (Q) factor, low acoustic losses, chemical stability and more importantly its compatibility with CMOS technology, which allow foundry process line and tool sharing, and open the way for system-on-chip integration^{1-5,7-9}. However, its rather low electromechanical coupling limits the bandwidth, which is one of the main challenges for its applications in wide band communication systems¹⁻⁶.

Recently large enhancement in piezo-response (d_{33}) and electromechanical coupling (K_{33}^2) has been discovered in Sc doped w -AlN¹⁰⁻¹². Interestingly, ferroelectricity with large electric polarization (~ 1 C/m²) has been predicted¹³ and recently demonstrated for Sc doping, al-

though the coercive field in the range of few MV/cm¹⁴, and the atomistic origin of this large coercive field is unclear. However, search for suitable dopants to replace Sc is of great scientific as well as industrial importance as Sc is an expensive and scarce element. In general, ions with high charge states (e.g., 4+ or 5+) can enhance ionic contribution to the piezoelectric stress constant e_{33} , hence might improve d_{33} . In this regard, based on density functional theory (DFT), a set of divalent cation (e.g., Mg²⁺, Ca²⁺ and Zn²⁺) and tetravalent cation (e.g., Hf⁴⁺, Zr⁴⁺, and Ti⁴⁺) has been predicted for significant enhancement of piezo-response in *w*-AlN^{15,16}. The ratio of divalent and tetravalent cations is kept 1:1 for the charge neutrality. In other words, two Al atoms are replaced by 1 divalent atom and 1 tetravalent atom. Recently, (Mg,Hf)_xAl_{1-x}N films (0 < *x* < 0.24) with a composition-gradient has been grown on a Si(100) substrate at 600°C by co-sputtering from AlN and MgHf targets¹⁷. This high-throughput/combinatorial approach for Mg and Hf co-doping has demonstrated a promisingly large piezo-response and power generation figure of merit suitable for energy harvesting¹⁷. Enhancement of piezoelectricity in several other quaternary alloys based on divalent and tetravalent cations in *w*-AlN (e.g., (Mg,Ti)AlN^{18,19}, (Mg,Zr)AlN^{20,21}, and (Zn,Ti)AlN¹⁹) has also been confirmed experimentally. Moreover, a giant increase of d_{33} in *w*-AlN by co-doping of divalent Mg and pentavalent Nb has been predicted by the first principles calculations²² and also later confirmed experimentally²³. The optimized atomic ratio between Nb⁵⁺ and Mg²⁺ ions in *w*-AlN is 1:2 for obtaining the best piezoelectric response²³ because this ratio ensures the charge neutrality. Furthermore, the co-doping of divalent and tetravalent/pentavalent in these cases are essential as the single dopants e.g., Mg^{19,23}, Zn¹⁹, Ti¹⁹, and Nb²³ in *w*-AlN not only have negative impact on the crystalline quality but also are ineffective for piezoelectricity enhancement. Note that aforementioned dopants in *w*-AlN are metastable and inaccessible through thermodynamic equilibrium synthesis process because of phase separation (e.g. rocksalt ScN and wurtzite AlN)^{11,13,17,18}. However, reactive magnetron sputtering, which is a physical vapor deposition (PVD) technique allows such metastable doping that broadens the compositional freedom for dopants, opening a large

possibility of designing new multi-functional materials^{11,13,17,18,24}.

Evidently, a general trend is choosing elements that show large ionic radius – preferably close to that of Sc^{3+} (88.5 pm) – and large charge state (e.g., 4+ or 5+) for enhancing piezo-response in $w\text{-AlN}$. This inspires us to study simultaneous doping of monovalent Li (ionic radius of 90pm) and pentavalent V/Nb/Ta (ionic radius of 68/78/78 pm, respectively) in 1:1 atomic ratio. Our first principles calculations show that this co-doping significantly improves the piezoelectric response of $w\text{-AlN}$. Our finding broadens compositional freedom to enhance the d_{33} in $w\text{-AlN}$, hence potential replacement of expensive Sc doping. Moreover, these co-doping introduces possibility of ferroelectricity in non-ferroelectric $w\text{-AlN}$. We estimate the coercive field (E_c) qualitatively, and find that the large E_c (in the range of few MV/cm) is due to the large energy difference between ferroelectric wurtzite and paraelectric hexagonal phase. Interestingly, the spontaneous electric polarization decreases as a function of co-doping concentration, although a quite large polarization (~ 0.80 C/m²) still remains at 37.5% co-doping, which is comparable to that of perovskites e.g PbTiO_3 . Additionally, we investigate various properties – namely elastic properties, electromechanical coupling, dielectric constant, and acoustic velocities – that are important parameters for designing piezoelectric devices such resonators, sensors, and energy harvesters. Promisingly, these properties are also quite comparable with these of Sc doped $w\text{-AlN}$.

Computational Details

Our first-principles calculations are performed in the framework of spin-polarized density functional theory using projector augmented wave (PAW) potentials to describe the core electrons and the generalized gradient approximation (GGA) of Perdew, Burke, and Ernzerhof (PBE) for exchange and correlation as implemented in the Vienna Ab initio Simulation Package (VASP)^{25–27} based on a plane-wave basis set. The number of valence electrons for Al, N, Li, V, Nb, and Ta are 3, 5, 1, 11, 11, and 11, respectively. On-site U corrections

(GGA+U) for d state of V, Nb and Ta are 3eV, 2.95eV and 2.95eV, respectively²⁸⁻³⁰. There is no magnetic moment observed, which is expected for pentavalent V, Nb and Ta ions. A cutoff energy of 500 eV for the plane-wave expansion is used in all calculations. All the structures are fully relaxed until the Hellmann-Feynman forces on each atom are less than 10^{-3} eV/. The lattice parameters and internal coordinates of the structures are fully relaxed to achieve the lowest energy configurations. Geometry optimization is carried out employing the conjugated gradient technique and the convergence for the total energy is set as 10^{-6} eV. The wurtzite supercells with 32 atoms are generated using the special quasirandom structures (SQS)³¹. For Li and X co-doped supercells, first we generate an SQS configuration at a particular concentration, then another configuration is generated by just interchanging the atomic positions of Li and X. For Sc doping, we consider an SQS supercell and a manually created supercell. The structural information of the relaxed supercells are given in the “Supplementary Information”. For both Sc and co-doping, all the results reported in this paper are average over the values obtained from the two considered supercells at a particular concentration. The Brillouin zone is sampled with a Γ -centered k -point mesh of $6 \times 6 \times 6$ for all the calculations. Density functional perturbation theory (DFPT) is used to calculate elastic C_{ij} , Born effective charges (Z_{ij}^*) and piezoelectric e_{ij} tensors. Using DFPT, we also qualitatively estimate the macroscopic dielectric constant (high frequency dielectric constant including local field effects or electronic contribution ϵ_{33}^∞ plus the static dielectric constant or ionic contribution ϵ_{33}^0).

Results and discussion

First, we examine how the doping changes the ratio of the lattice parameters a and c (i.e., c/a ratio) in w -AlN, which plays an important role in the origin of electric polarization as well as the piezoelectric response of wurtzites^{32,33}. Usually wurtzite crystals with smaller c/a ratio show higher piezoelectric response³². Our calculated c/a ratio of w -AlN (1.603)

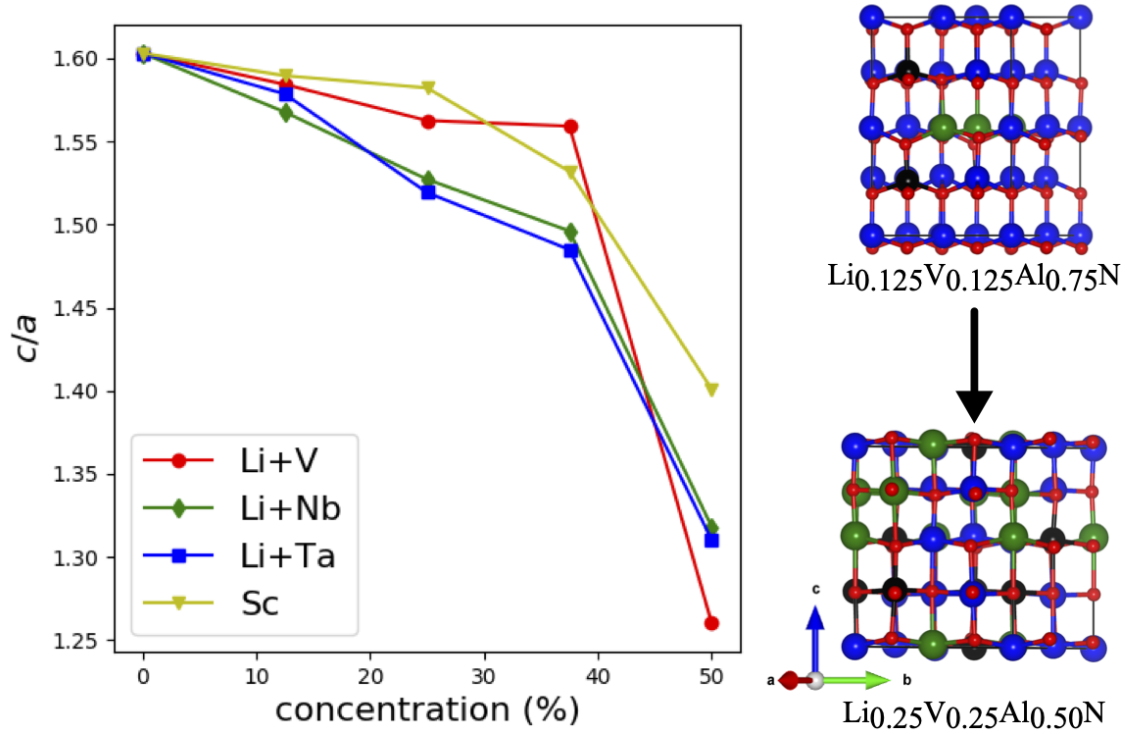


Figure 1: The change in c/a ratio as a function of doping concentration in w -AlN. The atomic structures of 25% and 50% Li and V co-doped w -AlN. The blue, red, green, and black balls represent Al, N, Li, and V atoms, respectively. The atomic planes of cations and anions for 50% co-doping are almost flat, and the structure resembles hexagonal BN structure. This also reflects in its low c/a ratio.

is comparable with the value of 1.587 obtained experimentally³⁴. The c/a ratio of w -AlN decreases as the doping concentration increases for both co-doping and Sc doping (see Figure 1). Both experiments and first principles calculations have already confirmed this decrease of the c/a ratio for Sc doping^{34,35} as well as other dopants^{15,23,36}. We notice a sharp drop in c/a ratio for all the co-doping above concentration of 37.5% (see Figure 1), indicating a phase transition from wurtzite to hexagonal (h -BN like structure) phase. For example, the c/a ratio of 50% Li and V co-doped structure is almost equal to that of h -AlN (1.24) (see Figure 1). Pictorially, we also see that the anions and cations in the optimized 50% Li and V co-doped structure are in almost same atomic-plane (i.e., flat plane), whereas they show wurtzite-like buckled atomic-layers for 25% co-doping (see Figure 1). Such structural change is also observed for Mg and Nb co-doping in w -AlN²³. Note that h -AlN exhibits neither spontaneous electric polarization nor piezoelectricity, although the doped h -AlN structures may show piezoelectric response because the doping lowers the symmetry locally. In this paper, we limit the doping concentration maximum of 37.5% as we mainly focus on the ferroelectricity and piezoelectricity.

We investigate the elastic properties of the single crystalline co-doped and Sc doped w -AlN. First, we check the mechanical stability under the co-doping. Elastic stiffness coefficients for a mechanically stable crystal satisfy Born stability criteria as the elastic energy must be positive. The elastic constants of the co-doped or Sc doped w -AlN should satisfy the stability criteria: $C_{11} > 0, (C_{11} - C_{12}) > 0, C_{44} > 0, (C_{11} + C_{12})C_{33} > 2C_{13}^2$ ³⁷. All our co-doped $\text{Li}_{x/2}\text{X}_{x/2}\text{Al}_{1-x}\text{N}$ and Sc doped $\text{Sc}_x\text{Al}_{1-x}\text{N}$ ($x=0-0.375$) structures satisfy the stability criteria (C_{11} , C_{12} , and C_{44} are provided in ‘‘Supplementary Information’’). The Figure 2(a) shows that all the co-dopants satisfy the $(C_{11} + C_{12})C_{33} > 2C_{13}^2$ criterion. However, generally it is difficult to grow single crystal, hence the single crystal elastic constants are not measured in experiments – rather usually some bulk elastic properties such as Young’s moduli (Y), bulk moduli (B), shear moduli (G) and Poisson ratio (ν) are measured. We use Voigt- Reuss-Hill scheme³⁸ based on the single crystal stiffness constants for calculating Y , B , G and ν . For

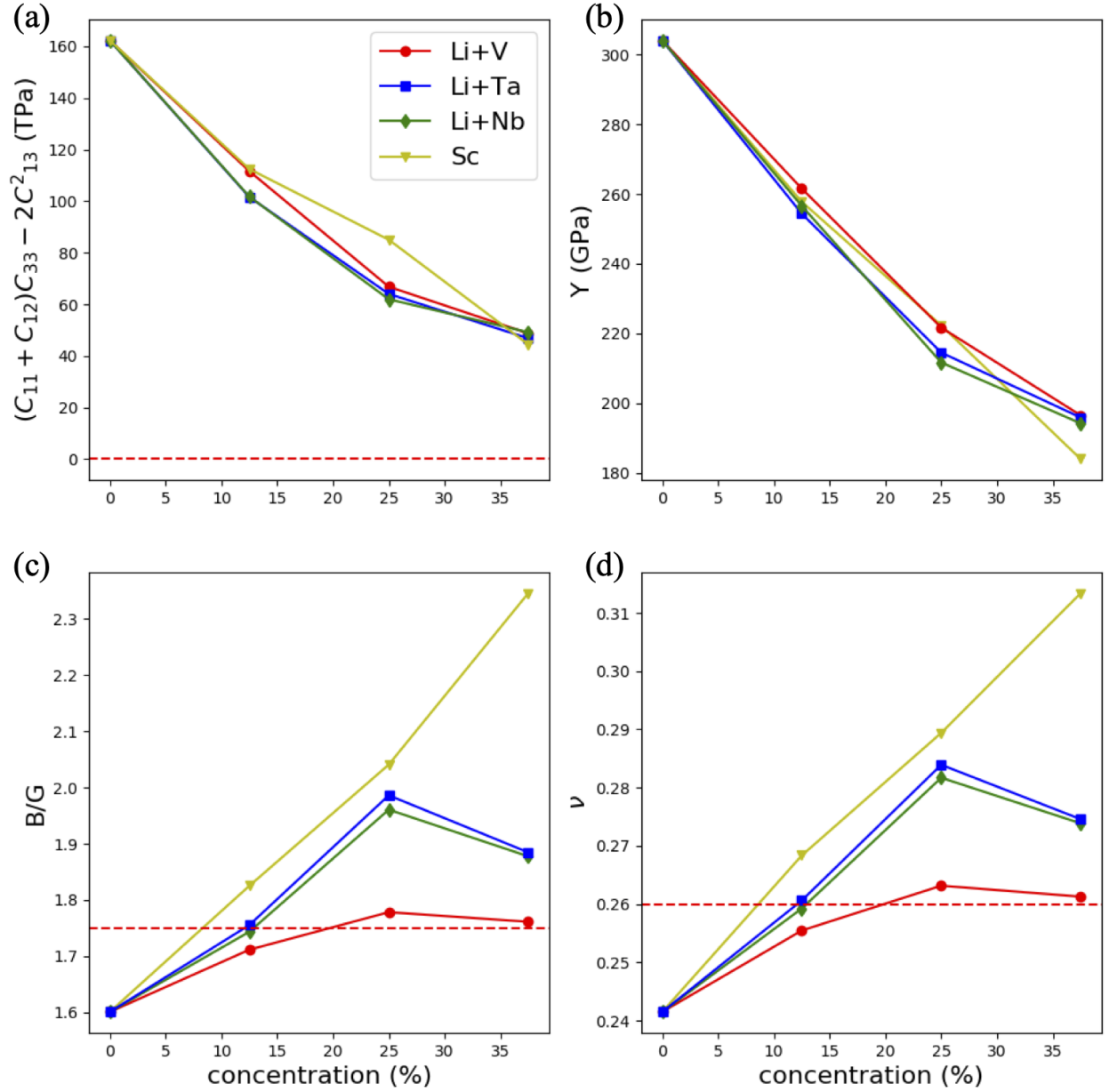


Figure 2: The Hill's average of (a) Young's modulus (Y), (b) Bulk modulus to shear modulus ratio (B/G), and (c) Poisson's ratio (ν) as a function of Sc and co-doping concentration in *w*-AlN. The Hill's average is employed for considering the polycrystallinity of the real doped materials. The red dotted line represents the critical value of B/G or ν that separate ductile from brittle behaviour of a material.

polycrystalline materials, the Voigt's (V) and the Reuss's (R) approximations provide the upper and lower bounds to the modulus, respectively. The Hill's average (H) is their arithmetic middle value, which is used in this work for the elastic properties of polycrystalline $\text{Li}_{x/2}\text{X}_{x/2}\text{Al}_{1-x}\text{N}$ and $\text{Sc}_x\text{Al}_{1-x}\text{N}$ ($x=0-0.375$) obtained from the ELATE code³⁸, shown in the Figure 2. All the co-dopants and Sc reduce the polycrystalline Young's modulus (Y), which is expected because the C_{33} decreases with increase in co-doping or Sc concentration. Our calculated Y for Sc doping is comparable with that of the experimentally reported values³⁹. Generally, the B/G ratio can be considered as a criterion for ductility or brittleness. The lower/higher the B/G ratio is, the more brittle/ductile the material is. The critical value for B/G is about 1.75, which separates ductile and brittle materials. Poisson ratio (ν) is another indicator of ductility or brittleness. Generally, materials with Poisson ratio lower (higher) than 0.26 are brittle (ductile). Interestingly, we find that both co-doping and Sc doping above 25% transforms brittle w -AlN to ductile (Figure 2(c,d)). In fact, Figure 2(b,c) shows that 37.5% Sc doping makes the w -AlN remarkably softer compared to the co-dopants.

We calculate total d_{33} and effective $d_{33,f}$ considering the relations $d_{ij} = \sum_{k=1}^6 e_{ik}(C^{-1})_{kj}$ and $d_{33,f} = e_{33}/C_{33}$, receptively, where d_{ij} , e_{ij} and C_{ij} are piezoelectric strain, piezoelectric stress and elastic tensors, respectively. In the definition of $d_{33,f}$, contributions from in-plane components of e_{ij} and C_{ij} tensors are ignored. It is assumed that the piezoelectric thin films can mainly change geometry along out-of-plane as the in-plane geometry change of the thin films is prevented by the rigidity of the substrate lattice⁴⁰. The d_{33} and the $d_{33,f}$ of w -AlN are 4.08 pC/N and 5.27 pC/N, respectively, which are in good agreement with the experimentally reported values of 4.0 pC/N and 5.56 pC/N, respectively⁴⁰. All the co-dopants increase both the total d_{33} and the $d_{33,f}$ of w -AlN (shown in Figure 3(a), (b)). For comparison, we calculate the d_{33} and the $d_{33,f}$ as function of Sc concentration in w - $\text{Sc}_x\text{Al}_{1-x}\text{N}$ ($x=0-0.375$), which are quite comparable with previously reported experimental^{10,11} and theoretical values^{12,35,41}. Additionally, Figure 3(a) shows a good agreement between our measured and calculated d_{33} for w -AlN as well as Sc doping. The samples were grown by

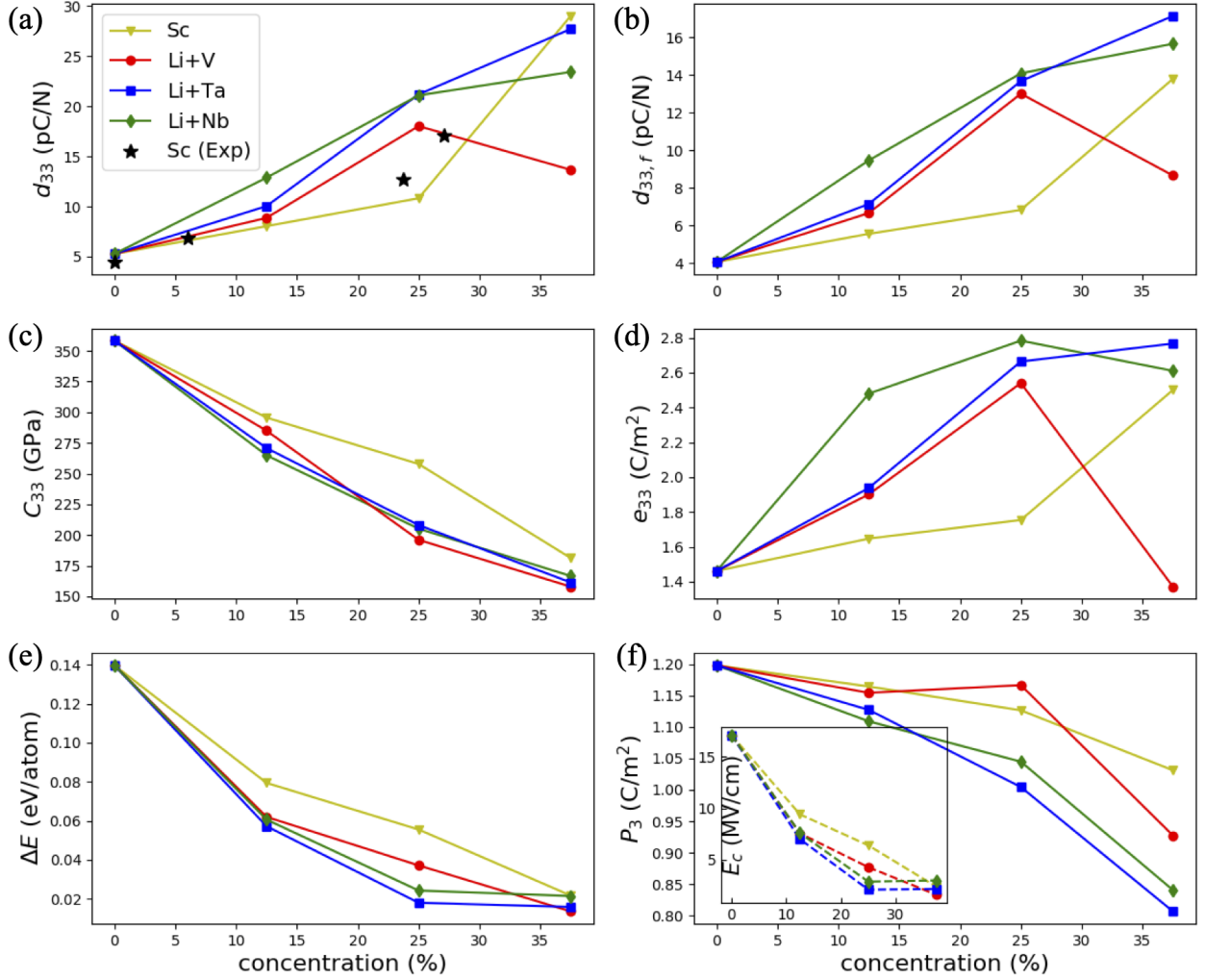


Figure 3: (a) The calculated piezoelectric strain constant d_{33} from the relation $d_{ij} = \sum_{k=1}^6 e_{ik}(C^{-1})_{kj}$, where all the components of piezoelectric stress constants (e_{ij}) and elastic constants (C_{ij}) contribute to d_{ij} , (b) the effective $d_{33,f} = e_{33}/C_{33}$, where it is assumed that the piezoelectric film is only operating along c -axis and the film is clamped to the substrate, (c) the elastic constant C_{33} , (d) the piezoelectric stress constants e_{33} , (e) the energy difference (ΔE) between the wurtzite and hexagonal (crystal structure of hexagonal Boron Nitride) phase of co-doped and Sc doped AlN, which is the estimated energy barrier for polarization switching and (f) the spontaneous electric polarization P_3 as a function of co-doping and Sc doping concentration in w -AlN. Experimental d_{33} for Sc doping in (a) are our own. The coercive field (E_c) as a function of concentration is shown in the inset of (f).

RF-sputtering, and the d_{33} is measured using a piezometer. We find that our highest total d_{33} for $\text{Li}_{0.1875}\text{Ta}_{0.1875}\text{Al}_{0.625}\text{N}$ is slightly lower than that of $\text{Sc}_{0.375}\text{Al}_{0.625}\text{N}$ (see Figure 3(a)). However, $d_{33,f}$ of $\text{Sc}_{0.375}\text{Al}_{0.625}\text{N}$ is about 3.34 pC/N lower than that of $\text{Li}_{0.1875}\text{Ta}_{0.1875}\text{Al}_{0.625}\text{N}$ (see Figure 3(b)), indicating that contributions from in-plane components of e_{ij} and C_{ij} tensors to d_{33} are larger in $\text{Sc}_{0.375}\text{Al}_{0.625}\text{N}$ compared to the co-dopants. In fact, d_{33} and $d_{33,f}$ of 12.5% Li and V/Nb/Ta co-doped w -AlN are also slightly larger than that of 12.5% Sc doped w -AlN (shown in Figure 3(b)). For example, compared to pure w -AlN ($d_{33,f} = 4.08$ pC/N), 12.5% Li+Nb co-doping ($d_{33,f} = 9.47$ pC/N) enhance $d_{33,f}$ about 132.1%, whereas Sc doping ($d_{33,f} = 5.57$ pC/N) enhances $d_{33,f}$ by 36.5%. Promisingly, all the co-dopants at 25% show significantly larger d_{33} and $d_{33,f}$ compared to these of 25% Sc doped w -AlN (see Figure 3(a-b)). Therefore, Li+V/Nb/Ta co-doping can be good alternatives of Sc doping in terms of piezoelectric response. Also, d_{33} and $d_{33,f}$ of these co-dopants in the doping range of 0-37.5% are quite comparable with these of other reported co-dopants e.g., 1pentavalent:1bivalent^{23,36} or 1tetraivalent:1bivalent^{15,16} co-doping.

The enhancement in d_{33} and $d_{33,f}$ is mainly due to the softening of elastic constant C_{33} and increase of e_{33} as the concentration of co-dopants increases (shown in Figure 3(c,d)). Similar mechanism is observed in other dopants e.g., Sc³⁵ or other dopants^{15,22,36}. Figure 1 indicates that these dopants lead the polar wurtzite structure close to a phase transition to non-polar hexagonal structure, which results in the softening of C_{33} ^{12,35}. In fact, the energy difference between wurtzite and hexagonal phase ($\Delta E = E_{\text{hexagonal}} - E_{\text{wurtzite}}$) becomes significantly smaller with the co-doping or Sc concentration – shown in Figure 3(e). This also indicates the energy proximity of the phase transition³⁵. Moreover, the ΔE can be considered as the energy barrier for ferroelectric polarization switching, where non-polar hexagonal phase acts as a paraelectric for a polarization switching from up to down. Obviously, the switching is assumed to occur by a uniform polarization change through a nonpolar high symmetry state, where formation of domains, effect of vacancies, effect of surface charges (depolarization field) in ultrathin films, and effect of electrodes are ignored for computa-

tional simplicity. Similar approach was also employed to predict ferroelectricity as well as to estimate ferroelectric switching barrier for hyperferroelectrics⁴² and Sc doped w -AlN¹³, which has been confirmed experimentally later¹⁴. Interestingly, switching energy barrier is tunable by doping concentration as it decreases with concentration (shown in Figure 3(e)). Also, our calculated energy barriers are comparable to these of Sc doped w -AlN¹³.

We calculate the spontaneous polarization by $P_3 = \frac{e}{V} \sum_k Z_{k,33}^* \Delta u_{k,3}$, where $Z_{k,33}^*$ is the 33 (3 represents crystal's c-direction) component of Born effective charge tensor of k -th atom in the supercell, $\Delta u_{k,3}$ is the atomic displacement along the c-direction of k -th atom with respect to the ideal nonpolar hexagonal configuration, e is the magnitude of an electron's charge and V is the polar supercell's volume^{14,43}. The calculated polarization as a function of co-doping and Sc doping concentration is shown in Figure 3(f). The polarization decreases with co-doping or Sc doping concentration, which is expected as the doping lowers the c/a ratio (see Figure 1) and leads the polar structures closer to the non-polar hexagonal structures. However, our obtained polarization values are quite comparable to that of perovskites e.g., PbTiO₃⁴⁴. Now, to qualitatively estimate the coercive field (E_c) from the energy barrier for the ferroelectric switching (ΔE), we express $E_c(t, T) = \frac{\Delta E - K_B T \ln(\frac{\vartheta_0 t}{\ln 2})}{V^* P_3}$, where t , T , K_B , ϑ_0 , V^* and P_3 represent the measurement time (t is set to 60s following the Ref¹⁴), temperature (300K), Boltzmann constant, the attempt frequency (10^{12} Hz, which is a typical optical phonon frequency), the volume of the elementary nucleation site (we consider the supercell as a nucleation site), and the spontaneous polarization, respectively⁴⁵. The estimated E_c are shown in the inset of Figure 3(f). Our estimated E_c (2.35 MV/cm) for 37.5% Sc doped w -AlN is quite comparable with that of experimentally measured value of about 2.5 MV/cm for 36% Sc doping¹³. We notice that the E_c decreases – expected as the ΔE decreases – when the Sc or the co-doping concentration increases (See Figure 3(e) and inset of 3(f)), which is also experimentally observed for Sc doping¹⁴. Interestingly, the E_c for 25% co-doping is much lower than that of 25% Sc doping, rather as low as that of 37.5% Sc doping, indicating the possibility of observing ferroelectric hysteresis loop using reasonable

electric field below about 2.5 MV/cm as beyond 4 MV/cm could not be physically realizable without damaging the samples adversely. However, a thorough investigation, beyond the scope of this paper, on the domain formations, the thickness dependence, and the surface effects will be needed for a deeper understanding. Note that the high E_c in the range of 0.8-2 MV/cm is reported for doped HfO_2 , where the large E_c is found beneficial for ferroelectric field-effect-transistors (FeFETs)^{46,47}. In ferroelectric HfO_2 , the low dielectric constant typically about 30 and the large E_c promotes ferroelectricity in the thickness range of 5–30 nm, which is usually very challenging for ferroelectric perovskites^{46,47}. Interestingly, we find that Sc doped as well as the co-doped $w\text{-AlN}$ also show as low dielectric constant (see Figure 5(b)) as that of ferroelectric HfO_2 . Therefore, these doped $w\text{-AlN}$ can be promising ferroelectrics at nanoscale.

To understand the origin of the e_{33} enhancement, we express e_{33} ($e_{33}=e_{33}^{ele}+e_{33}^{int}$) in terms of (i) the electronic contribution (e_{33}^{ele}) and (ii) the contribution from the internal coordinates of atoms (e_{33}^{int}) in response to an external strain along c -direction (η_3)^{16,43,48}. We find that the large increase of e_{33} is the result of simultaneous significant increase in e_{33}^{int} but decrease in the magnitude of e_{33}^{ele} as a function of co-doping concentration (see Figure 4(a-b)). In contrast, the $|e_{33}^{ele}|$ of Sc doping slightly increases with concentration (see Figure 4(b)) – in agreement with the previous calculations³⁵. In fact, the $e_{33}^{int}(|e_{33}^{ele}|)$ for all the co-dopants at 25% concentration is quite significantly larger (smaller) than that of the Sc doped $w\text{-AlN}$, which guarantees the larger e_{33} (Fig.3(d)) for the co-doping compared to that of 25% Sc doping. From Fig.4(a-b), we see that the sudden big drop in e_{33} for 37.5% Li and V co-doping is solely due to the significant decrease of the e_{33}^{int} as the e_{33}^{ele} remains almost unchanged. For further insights, note that the e_{33}^{int} is proportional to the Born effective charge (Z_{33}) of the ions and the sensitivity ($\frac{du_3}{d\eta_3}$) of the atomic positions (u_3) in response to the strain along c -direction (η_3). For the wurtzite structure, the e_{33}^{int} equals to $\sum_i \frac{2e}{\sqrt{3}a_s^2} Z_{33}(i) \frac{du_3(i)}{d\eta_3}$, where i runs over all the atoms in the supercell, a_s is the in-plane lattice parameter of the supercell, and e is the electron charge^{16,43,48}. It is convenient to consider an average value of Z_{33} and $\frac{du_3}{d\eta_3}$,

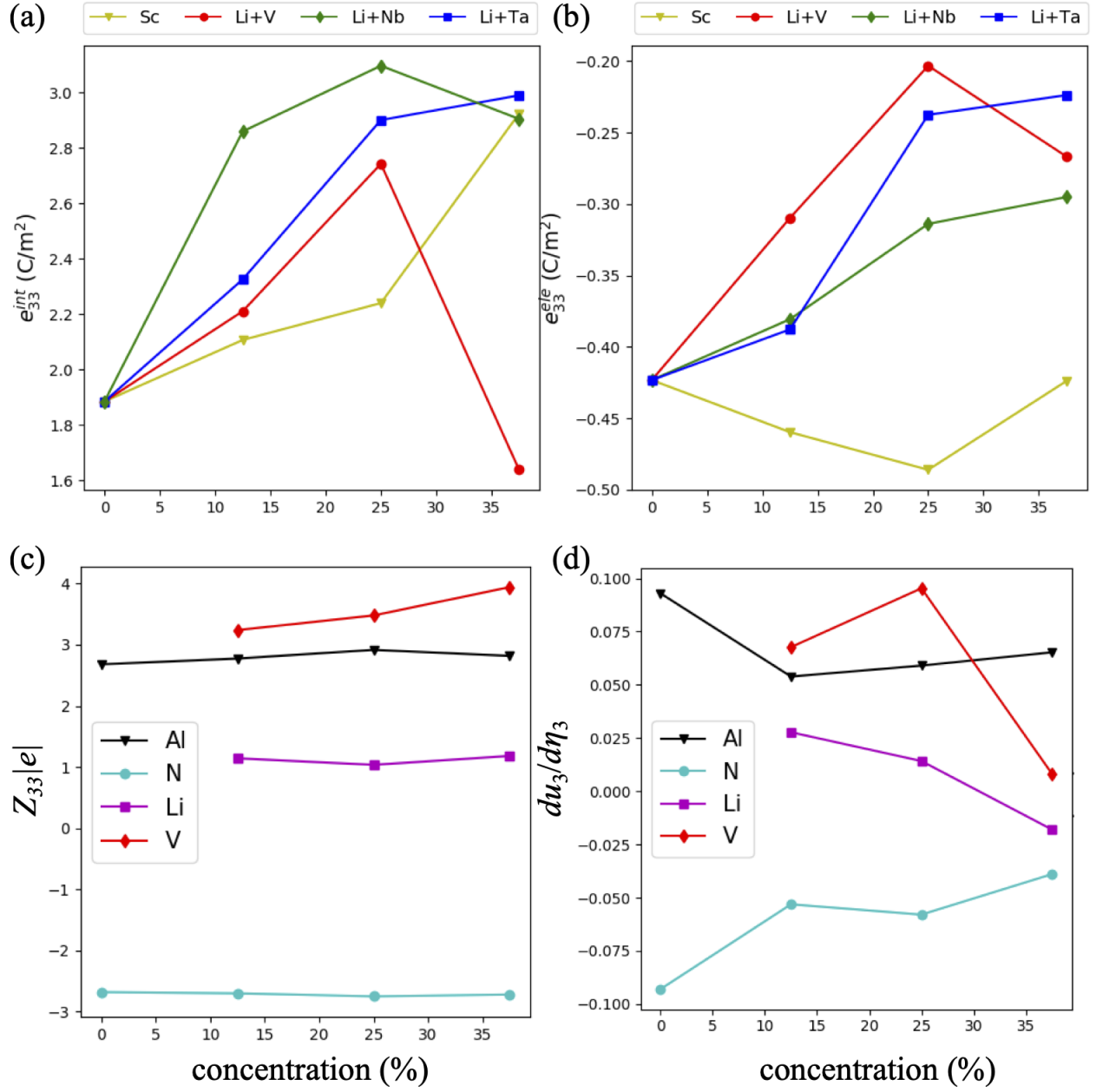


Figure 4: (a) The internal coordinate (e_{33}^{int}) and (b) the electronic (e_{33}^{ele}) parts of the e_{33} as a function of doping concentration. The simultaneous significant increase in e_{33}^{int} but decrease in the magnitude of e_{33}^{ele} result enhancement in e_{33} for co-doping. The e_{33}^{int} is proportional to (c) the 33 component of Born effective charge (Z_{33}) tensor and (d) the ($\frac{du_3}{d\eta_3}$), which is the sensitivity of the atomic positions (u_3) in response to a strain along c -direction (η_3). Although the Z_{33} remains almost unchanged for Li and V co-doping as a function of concentration, the $\frac{du_3}{d\eta_3}$ of both Li and V drops significantly at 37.5%, which consequently results a dramatic drop in total e_{33} .

rather than these of the individual atoms in a large supercell. In Figure 4(c), we show average Z_{33} for each type of atom (k) in the supercell, which is defined as $Z_{33}(k) = \frac{1}{Nn_k} \sum_N \sum_{n_k} Z_{33}(n_k)$, where N represents the number of supercells considered for each concentration (we use 2 supercells for each doping/co-doping concentration, hence $N=2$), n_k runs over all the k -type atoms in a supercell (e.g., n_{Al} , n_{N} , n_{Li} and $n_{\text{V/Nb/Ta}}$ are 10, 16, 3 and 3 for 37.5% Li and V/Nb/Ta co-doping, respectively). Similarly, we also take average of $\frac{du_3}{d\eta_3}$, which is defined as $\frac{du_3(k)}{d\eta_3} = \frac{1}{Nn_k} \sum_N \sum_{n_k} \frac{du_3(n_k)}{d\eta_3}$. We find that the large increase in the e_{33}^{int} for co-doping is due to the large Z_{33} of the V/Nb/Ta and the enhancement of $\frac{du_3}{d\eta_3}$ compared to these of w -AlN (see Figure S.1 and Figure S.2 in the supplementary materials). Now, from Figure 4(c-d), we notice that the Z_{33} remains almost unchanged for Li and V co-doping as a function of concentration, although the $\frac{du_3}{d\eta_3}$ of both Li and V drops significantly at 37.5%, which consequently results a dramatic drop in the e_{33}^{int} , hence also in the total e_{33} .

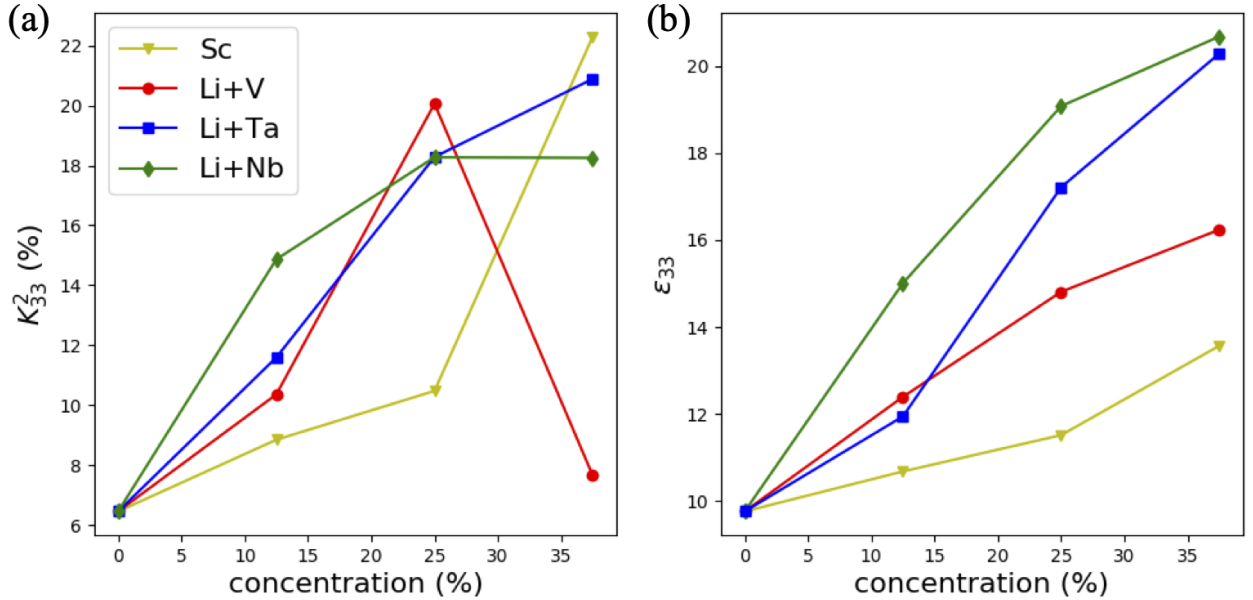


Figure 5: (a) The longitudinal electromechanical coupling constant (K_{33}^2) and (b) the zz component of the macroscopic dielectric tensor ϵ_{33} as a function of co-doping and Sc doping concentration in w -AlN.

Piezoelectric materials used in various applications e.g., transducers, energy harvesting, pressure sensors, gyroscopes, and accelerometer operate in the longitudinal vibration mode. Generally a high value of the electromechanical coupling coefficient K_{33}^2 is required for trans-

ducers with broader band-width, better axial resolution, and better sensitivity. K_{33}^2 , shown in Figure 5(a), is defined as $K_{33}^2 = \frac{e_{33}^2}{\epsilon_{33}C_{33} + e_{33}^2} \times 100\%$, where ϵ_{33} is a component of the dielectric tensor (shown in Figure 5(b))⁴⁹. We find that Sc and all co-dopants significantly enhance K_{33}^2 (Figure 5(a)). Our calculated K_{33}^2 values for Sc doping is consistent with the values reported experimentally^{50,51}. For example, the experimentally estimated electromechanical coupling coefficients for Sc doping of 20% and 30% are 10% and 15%, respectively⁵¹. 37.5% co-doping of Li and Ta in a 1:1 ratio shows the highest K_{33}^2 (20.89%), which is 3.24 times larger than that of pure *w*-AlN. The low K_{33}^2 for Li and V co-doping at 37.5% is due to its decrease in e_{33} (shown in Figure 3(d)). Note that K_{33}^2 of all the co-dopants at 37.5% are lower than that of Sc doped *w*-AlN mainly because ϵ_{33} for Sc doping does not increase much as the Sc concentration increases (shown in Figure 5(b)). Similar values and trend of increase in ϵ_{33} ⁵¹ or effective ϵ_{33} , measured for the thin films clamped to the substrate, has also been observed for Sc doping experimentally³⁴. Our calculated ϵ_{33} for *w*-AlN is also close to typical experimental values (~ 10) in the literature^{34,51}. In general, the K_{33}^2 for a device depends collectively on the materials properties of the piezoelectric, the electrodes, and the device design. Here, it should also be mentioned that a high value of $K_{33}^2 \cdot Q$ is desired for a resonator with high performance and wide bandwidth, where Q is the mechanical quality factor. The Q determines the loss of an inserted mechanical energy. Generally, the Q is proportional to the stiffness constants⁵², although several damping mechanisms e.g, damping at the interface between the piezoelectric and the electrodes, the phonon-phonon dissipation, damping due the quality of the piezoelectric (e.g., scattering of the acoustic wave by the defects), and mechanical energy leakage due to the device fabrication have significant impact^{53,54}. As the C_{33} decreases with the doping concentration, hence we expect a decrease in the Q . Indeed, this has been observed experimentally for Sc⁶ and other co-dopants⁵⁵.

For many piezoelectric-based actuators, energy harvesters, and sensors, transverse piezoelectric coefficient d_{31} is also an important parameter, and a large d_{31} is desired. We find that co-doping significantly enhances the d_{31} compared to that of pure *w*-AlN (Shown in Figure

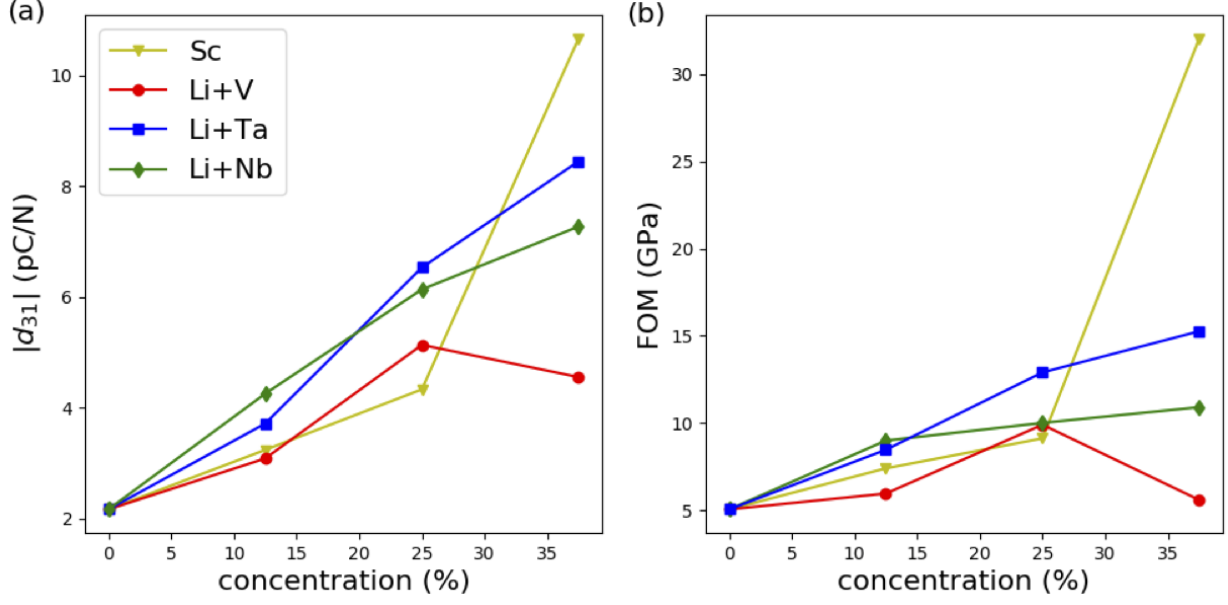


Figure 6: (a) the magnitude of the transverse piezoelectric strain constant (d_{31}) and (b) the figure of merit (FOM) for piezoelectric power generation as a function of Sc and co-doping concentration in w -AlN.

6(a)). Note that d_{31} and d_{32} are equal in pure w -AlN due to its crystal symmetry (space group $P6_3mc$). However, doping locally breaks the symmetry, hence d_{31} and d_{32} are not exactly equal, although they are close in value (See “Supplementary Information”). We can therefore take as a reasonable approximation the average of d_{31} and d_{32} for estimating d_{31} . Note that we also consider two configurations for each co-doping or Sc doping concentration – discussed in the computational details section. Therefore, the reported d_{31} is also the average d_{31} of two configurations at each concentration. 37.5% co-doping of Li and Ta shows the highest d_{31} (-8.45 pC/N), which is about 3.89 times larger than that of pure w -AlN, whereas d_{31} for 37.5% Sc doping is -10.67 pC/N. Larger d_{31} usually guarantees higher figure of merit (FOM), which is an another important parameter for choosing piezoelectric materials for power generation in vibration-based energy harvesters. FOM is defined as $FOM = \frac{d_{31}^2 Y^2}{\epsilon_{33}}$, where Y is the Hill’s Young’s modulus (see Figure 2(b))¹⁷. We find that the co-dopants significantly enhance the FOM compared to that of w -AlN. This is especially obvious for Li and Ta co-doping (see Fig.6(b)). For 37.5% Li and Ta co-doping the FOM is 16.60 GPa,

which is 3.27 times higher than that of w -AlN. This is promising for energy harvesters. Due to the low d_{31} the FOM for 37.5% Li and V co-doping, 5.91 GPa, is lower than that for 25% co-doping (10.23 GPa). But this is still twice that of w -AlN. Note that because of low ε_{33} of Sc doped w -AlN (see Figure 5(b)), the FOM of Sc doped w -AlN remains higher than that of the co-dopants for the considered concentration range.

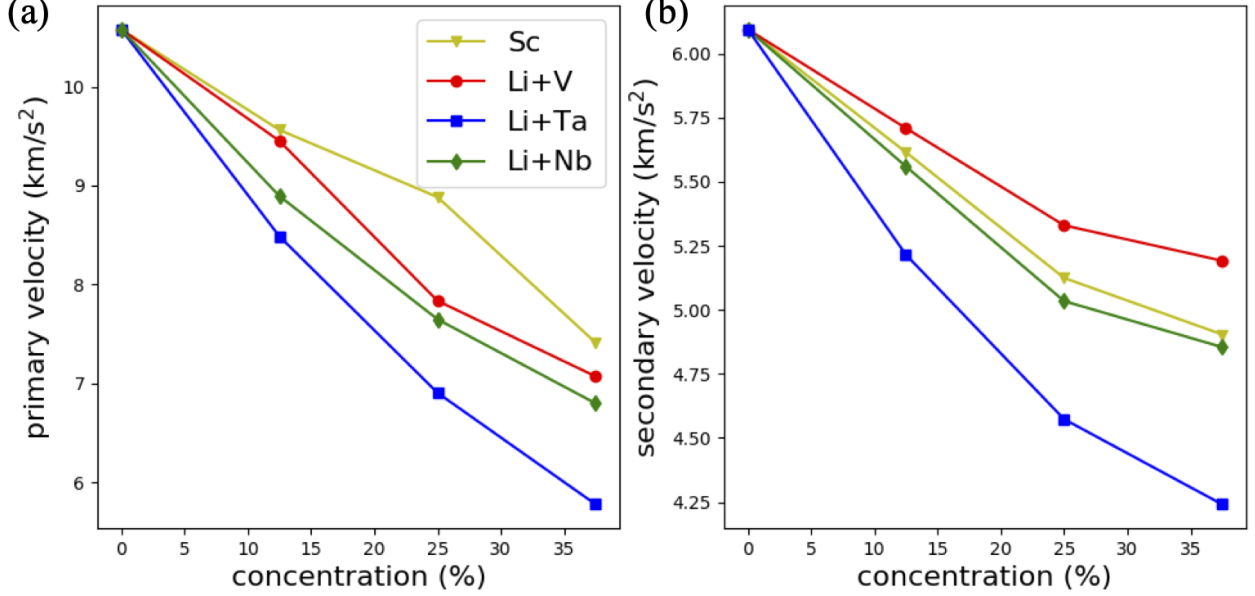


Figure 7: (a) The primary (longitudinal) and (b) the average secondary (transverse) acoustic velocity as a function of Sc and co-doping concentration in w -AlN.

For designing electroacoustic devices e.g. film-bulk acoustic resonators (FBARs) or surface acoustic wave (SAW) resonators for their applications in the frequency filters and duplexers for next generation wireless communication systems, the acoustic wave velocity is an important parameter, which is also sometimes used to estimate the elastic constants in experiments. Compared to other piezoelectrics^{53,56}, a high acoustic wave velocity of w -AlN is one of the key advantages for high frequency SAW resonators. We compute the elastic wave velocity by solving Christoffel equation $(C_{ijkl}\eta_j\eta_k - \rho v^2\delta_{ij})u_l = 0$, where C_{ijkl} is the elastic co-efficient factor, η represents the propagation direction of the wave, ρ is the mass density, v is the velocity and u stands for the wave polarization⁵⁷. For a given direction, there are three solutions (three velocities): a longitudinal velocity, also known as primary

velocity (v_P), when the wave polarization is parallel to the wave propagation direction and two transverse velocities, known as secondary velocities (v_S), when the wave polarization is perpendicular to the wave propagation direction⁵⁷. Figure 7 shows the calculated elastic wave velocities along the [001] direction, which is usually the important direction for designing devices e.g., resonators or sensors. Our calculated v_P and v_S for w -AlN are 10.58 Km/s² and 6.10 Km/s², respectively, which are in good agreement with the values in the literature^{50,58}. We find that co-doping and Sc doping decrease both the primary and the secondary wave velocities as the doping concentration increases –again due to the decrease in C_{33} with the doping concentration. This trend is also observed experimentally for Sc doping⁵⁰ and Mg and Hf/Zr co-doping²¹. Li and Ta co-doping shows the lowest velocities, which mainly due to the fact that Ta is the heaviest among our considered elements. The velocities at any particular concentration of our considered co-dopants are quite comparable with these of Sc doped w -AlN, and also comparable with the velocities in the range of 5-7 km/s for LiNbO₃ or LiTaO₃ crystals depending on the cuts^{53,56}.

Conclusion

We show that Li and X (X=V, Nb and Ta) co-doping in 1Li:1X ratio significantly enhances the piezoelectric constants (d_{33} and d_{31}), electromechanical coupling constant (K_{33}^2), and figure of merit for power generation of w -AlN, which make these co-doped w -AlN are potential lead-free piezoelectric materials for energy harvesting, sensors, and resonators for high frequency RF signals. These parameters are also quite comparable with these of Sc doped w -AlN. In fact, these co-dopants outperform Sc doping in terms of piezo-response – especially at 25% concentration – promising that the co-dopants can be good alternative of expensive Sc. Interestingly, the co-doped w -AlN also show the possibility of ferroelectric polarization switching with a quite large spontaneous electric polarization about 0.80 C/m² with large coercive field of few MV/cm but relatively low dielectric constant of about 20, opening new

possibilities in wurtzite nitrides for nanoscale memory applications. Increase in piezoelectric stress constant (e_{33}) with decrease in elastic constant (C_{33}) results enhancement in piezoelectric strain constant (d_{33}). However, the enhancement in K_{33}^2 is not as pronounced as that in d_{33} , because co-doping increases dielectric constant. The longitudinal acoustic wave velocity drops with co-doping or Sc concentration, although the velocity is still comparable with that of commercially used piezoelectric LiNbO_3 or LiTaO_3 in special cuts.

Acknowledgment This publication has emanated from research conducted with the financial support of Science Foundation Ireland (SFI) and is co-funded under the European Regional Development Fund under Grant Number 13/RC/2077. MN acknowledges support from SFI through grant number 17/NSFC/5279. The calculations were performed using the high-performance computing facilities of the Tyndall National Institute. We also acknowledge access to computing resources at Irish Centre for High-End Computing (ICHEC).

References

- (1) Loebl, H. P.; Klee, M.; Metzmacher, C.; Brand, W.; Milsom, R.; Lok, P. Piezoelectric thin AlN films for bulk acoustic wave (BAW) resonators. *Mater. Chem. Phys.* **2003**, *79*, 143 – 146.
- (2) Muralt, P.; Antifakos, J.; Cantoni, M.; Lanz, R.; Martin, F. Is there a better material for thin film BAW applications than AlN? *IEEE Ultrasonics Symposium* **2005**, *1*, 315–320.
- (3) Karabalin, R. B.; Matheny, M. H.; Feng, X. L.; Defaÿ, E.; Rhun, G. L.; Marcoux, C.; Hentz, S.; Andreucci, P.; Roukes, M. L. Piezoelectric nanoelectromechanical resonators based on aluminum nitride thin films. *Appl. Phys. Lett.* **2009**, *95*, 103111.
- (4) Xiong, C.; Sun, X.; Fong, K. Y.; Tang, H. X. Integrated high frequency aluminum nitride optomechanical resonators. *Appl. Phys. Lett.* **2012**, *100*, 171111.

- (5) Rinaldi, M.; Zuniga, C.; Zuo, C.; Piazza, G. Super-high-frequency two-port AlN contour-mode resonators for RF applications. *IEEE Transactions on Ultrasonics, Ferroelectrics, and Frequency Control* **2010**, *57*, 38–45.
- (6) Park, M.; Hao, Z.; Kim, D. G.; Clark, A.; Dargis, R.; Ansari, A. A 10 GHz Single-Crystalline Scandium-Doped Aluminum Nitride Lamb-Wave Resonator. 20th International Conference on Solid-State Sensors, Actuators and Microsystems Eurosensors XXXIII (Transducers Eurosensors XXXIII). 2019; pp 450–453.
- (7) Piazza, G.; Felmetzger, V.; Muralt, P.; Olsson III, R. H.; Ruby, R. Piezoelectric aluminum nitride thin films for microelectromechanical systems. *MRS Bulletin* **2012**, *37*, 1051–1061.
- (8) Sinha, N.; Wabiszewski, G. E.; Mahameed, R.; Felmetzger, V. V.; Tanner, S. M.; Carpick, R. W.; Piazza, G. Piezoelectric aluminum nitride nanoelectromechanical actuators. *Appl. Phys. Lett.* **2009**, *95*, 053106.
- (9) Campanella, H.; Qian, Y.; Romero, C. O.; Giner, J.; Kumar, R. Monolithic MEMS Filter Banks on RFSOI Front-End Module. *2020 IEEE 33rd International Conference on Micro Electro Mechanical Systems (MEMS)* **2020**, 218–221.
- (10) Akiyama, M.; Kamohara, T.; Kano, K.; Teshigahara, A.; Takeuchi, Y.; Kawahara, N. Enhancement of Piezoelectric Response in Scandium Aluminum Nitride Alloy Thin Films Prepared by Dual Reactive Cosputtering. *Adv. Mater.* **2009**, *21*, 593–596.
- (11) Talley, K. R.; Millican, S. L.; Mangum, J.; Siol, S.; Musgrave, C. B.; Gorman, B.; Holder, A. M.; Zakutayev, A.; Brennecke, G. L. Implications of heterostructural alloying for enhanced piezoelectric performance of (Al,Sc)N. *Phys. Rev. Materials* **2018**, *2*, 063802.
- (12) Tholander, C.; Abrikosov, I. A.; Hultman, L.; Tasnádi, F. Volume matching condition to

- establish the enhanced piezoelectricity in ternary $(\text{Sc,Y})_{0.5}(\text{Al,Ga,In})_{0.5}\text{N}$ alloys. *Phys. Rev. B* **2013**, *87*, 094107.
- (13) Zhang, S.; Holec, D.; Fu, W. Y.; Humphreys, C. J.; Moram, M. A. Tunable optoelectronic and ferroelectric properties in Sc-based III-nitrides. *J. Appl. Phys.* **2013**, *114*, 133510.
 - (14) Fichtner, S.; Wolff, N.; Lofink, F.; Kienle, L.; Wagner, B. AlScN: A III-V semiconductor based ferroelectric. *J. Appl. Phys.* **2019**, *125*, 114103.
 - (15) Iwazaki, Y.; Yokoyama, T.; Nishihara, T.; Ueda, M. Highly enhanced piezoelectric property of co-doped AlN. *Appl. Phys. Express* **2015**, *8*, 061501.
 - (16) Tholander, C.; Tasnádi, F.; Abrikosov, I. A.; Hultman, L.; Birch, J.; Alling, B. Large piezoelectric response of quarternary wurtzite nitride alloys and its physical origin from first principles. *Phys. Rev. B* **2015**, *92*, 174119.
 - (17) Nguyen, H. H.; Oguchi, H.; Minh, L. V.; Kuwano, H. High-Throughput Investigation of a Lead-Free AlN-Based Piezoelectric Material, $(\text{Mg,Hf})_x\text{Al}_{1-x}\text{N}$. *ACS Comb. Sci.* **2017**, *19*, 365–369.
 - (18) Wang, B.; Aryana, K.; Gaskins, J. T.; Hopkins, P. E.; Khare, S. V.; Gall, D. Structural Stabilization and Piezoelectric Enhancement in Epitaxial $(\text{Ti}_{1-x}\text{Mg}_x)_{0.25}\text{Al}_{0.75}\text{N}(0001)$ Layers. *Adv. Funct. Mater.* **2020**, *30*, 2001915.
 - (19) Anggraini, S. A.; Uehara, M.; Hirata, K.; Yamada, H.; Akiyama, M. Effects of different divalent cations in mTi-based codopants ($m = \text{Mg}$ or Zn) on the piezoelectric properties of AlN thin films. *Ceram. Int.* **2020**, *46*, 4015 – 4019.
 - (20) Minh, L. V.; Hara, M.; Yokoyama, T.; Nishihara, T.; Ueda, M.; Kuwano, H. Highly piezoelectric MgZr co-doped aluminum nitride-based vibrational energy harvesters

- [Correspondence]. *IEEE Transactions on Ultrasonics, Ferroelectrics, and Frequency Control* **2015**, *62*, 2005–2008.
- (21) Nagakubo, A.; Arita, M.; Yokoyama, T.; Matsuda, S.; Ueda, M.; Ogi, H.; Hirao, M. Acoustic properties of co-doped AlN thin films at low temperatures studied by picosecond ultrasonics. *Jpn. J. Appl. Phys.* **2015**, *54*, 07HD01.
 - (22) Hirata, K.; Yamada, H.; Uehara, M.; Anggraini, S. A.; Akiyama, M. First-Principles Study of Piezoelectric Properties and Bonding Analysis in (Mg, X, Al)N Solid Solutions (X = Nb, Ti, Zr, Hf). *ACS Omega* **2019**, *4*, 15081–15086.
 - (23) Uehara, M.; Shigemoto, H.; Fujio, Y.; Nagase, T.; Aida, Y.; Umeda, K.; Akiyama, M. Giant increase in piezoelectric coefficient of AlN by Mg-Nb simultaneous addition and multiple chemical states of Nb. *Appl. Phys. Lett.* **2017**, *111*, 112901.
 - (24) Holder, A. M. et al. Novel phase diagram behavior and materials design in heterostructural semiconductor alloys. *Sci. Adv.* **2017**, *3*.
 - (25) Perdew, J. P.; Burke, K.; Ernzerhof, M. Generalized Gradient Approximation Made Simple. *Phys. Rev. Lett.* **1996**, *77*, 3865.
 - (26) Kresse, G.; Furthmüller, J. Efficient iterative schemes for ab initio total-energy calculations using a plane-wave basis set. *Phys. Rev. B* **1996**, *54*, 11169.
 - (27) Kresse, G.; Joubert, D. From ultrasoft pseudopotentials to the projector augmented-wave method. *Phys. Rev. B* **1999**, *59*, 1758.
 - (28) Calandra, M. Phonon-Assisted Magnetic Mott-Insulating State in the Charge Density Wave Phase of Single-Layer 1T–NbSe₂. *Phys. Rev. Lett.* **2018**, *121*, 026401.
 - (29) Martino, E.; Pisoni, A.; Ćirić, L.; Arakcheeva, A.; Berger, H.; Akrap, A.; Putzke, C.; Moll, P. J. W.; Batistić, I.; Tutiš, E.; Forró, L.; Semeniuk, K. Preferential out-of-plane

- conduction and quasi-one-dimensional electronic states in layered $1T\text{-TaS}_2$. *npj 2D Mater. and Appl.* **2020**, *4*, 7.
- (30) Wang, Y.; Puggioni, D.; Rondinelli, J. M. Assessing exchange-correlation functional performance in the chalcogenide lacunar spinels GaM_4Q_8 ($M = \text{Mo, V, Nb, Ta}$; $Q = \text{S, Se}$). *Phys. Rev. B* **2019**, *100*, 115149.
- (31) van de Walle, A.; Tiwary, P.; de Jong, M.; Olmsted, D.; Asta, M.; Dick, A.; Shin, D.; Wang, Y.; Chen, L.-Q.; Liu, Z.-K. Efficient stochastic generation of special quasirandom structures. *Calphad* **2013**, *42*, 13 – 18.
- (32) Momida, H.; Oguchi, T. Effects of lattice parameters on piezoelectric constants in wurtzite materials: A theoretical study using first-principles and statistical-learning methods. *Appl. Phys. Express* **2018**, *11*, 041201.
- (33) Nann, T.; Schneider, J. Origin of permanent electric dipole moments in wurtzite nanocrystals. *Chem. Phys. Lett.* **2004**, *384*, 150 – 152.
- (34) Kurz, N.; Ding, A.; Urban, D. F.; Lu, Y.; Kirste, L.; Feil, N. M.; Žukauskaitė, A.; Ambacher, O. Experimental determination of the electro-acoustic properties of thin film AlScN using surface acoustic wave resonators. *J. Appl. Phys.* **2019**, *126*, 075106.
- (35) Tasnádi, F.; Alling, B.; Höglund, C.; Wingqvist, G.; Birch, J.; Hultman, L.; Abrikosov, I. A. Origin of the Anomalous Piezoelectric Response in Wurtzite $\text{Sc}_x\text{Al}_{1-x}\text{N}$ Alloys. *Phys. Rev. Lett.* **2010**, *104*, 137601.
- (36) Tagami, K.; Koga, J.; Nohara, Y.; Usami, M. Origin of enhanced piezoelectric constants of MgNbAlN studied by first-principles calculations. *Jpn. J. Appl. Phys.* **2017**, *56*, 058004.
- (37) Mouhat, F.; Coudert, F. Necessary and sufficient elastic stability conditions in various crystal systems. *Phys. Rev. B* **2014**, *90*, 224104.

- (38) Gaillac, R.; Pullumbi, P.; Coudert, F. ELATE: an open-source online application for analysis and visualization of elastic tensors. *J. Phys. Condens. Matter* **2016**, *28*, 275201.
- (39) Akiyama, M.; Umeda, K.; Honda, A.; Nagase, T. Influence of scandium concentration on power generation figure of merit of scandium aluminum nitride thin films. *Appl. Phys. Lett.* **2013**, *102*, 021915.
- (40) Dubois, M.; Muralt, P. Stress and piezoelectric properties of aluminum nitride thin films deposited onto metal electrodes by pulsed direct current reactive sputtering. *J. Appl. Phys.* **2001**, *89*, 6389–6395.
- (41) Momida, H.; Teshigahara, A.; Oguchi, T. Strong enhancement of piezoelectric constants in $\text{Sc}_x\text{Al}_{1-x}\text{N}$: First-principles calculations. *AIP Adv.* **2016**, *6*, 065006.
- (42) Bennett, J. W.; Garrity, K. F.; Rabe, K. M.; Vanderbilt, D. Hexagonal *ABC* Semiconductors as Ferroelectrics. *Phys. Rev. Lett.* **2012**, *109*, 167602.
- (43) Noor-A-Alam, M.; Olszewski, O. Z.; Nolan, M. Ferroelectricity and Large Piezoelectric Response of AlN/ScN Superlattice. *ACS Appl. Mater. Interfaces* **2019**, *11*, 20482–20490.
- (44) Tuttle, B. A.; Payne, D. A.; Mukherjee, J. L. Spontaneous Polarization for Ferroelectric Materials. *MRS Bulletin* **1994**, *19*, 20–20.
- (45) Vopsaroiu, M.; Blackburn, J.; Cain, M. G.; Weaver, P. M. Thermally activated switching kinetics in second-order phase transition ferroelectrics. *Phys. Rev. B* **2010**, *82*, 024109.
- (46) Mikolajick, T.; Slesazeck, S.; Park, M. H.; Schroeder, U. Ferroelectric hafnium oxide for ferroelectric random-access memories and ferroelectric field-effect transistors. *MRS Bulletin* **2018**, *43*, 340–346.
- (47) Fan, Z.; Chen, J.; Wang, J. Ferroelectric HfO_2 -based materials for next-generation ferroelectric memories. *J. Adv. Dielectr.* **2016**, *06*, 1630003.

- (48) Bernardini, F.; Fiorentini, V.; Vanderbilt, D. Spontaneous polarization and piezoelectric constants of $III - V$ nitrides. *Phys. Rev. B* **1997**, *56*, R10024–R10027.
- (49) Manna, S.; Brennecka, G. L.; Stevanović, V.; Ciobanu, C. V. Tuning the piezoelectric and mechanical properties of the AlN system via alloying with YN and BN. *J. Appl. Phys.* **2017**, *122*, 105101.
- (50) Yanagitani, T.; Suzuki, M. Electromechanical coupling and gigahertz elastic properties of ScAlN films near phase boundary. *Appl. Phys. Lett.* **2014**, *105*, 122907.
- (51) Wingqvist, G.; Tasnádi, F.; Zukauskaitė, A.; Birch, J.; Arwin, H.; Hultman, L. Increased electromechanical coupling in $w\text{-Sc}_x\text{Al}_{1-x}\text{N}$. *Appl. Phys. Lett.* **2010**, *97*, 112902.
- (52) Wu, D.; Chen, Y.; Manna, S.; Talley, K.; Zakutayev, A.; Brennecka, G. L.; Ciobanu, C. V.; Constantine, P.; Packard, C. E. Characterization of Elastic Modulus Across the $(\text{Al}_{1-x}\text{Sc}_x)\text{N}$ System Using DFT and Substrate-Effect-Corrected Nanoindentation. *IEEE Transactions on Ultrasonics, Ferroelectrics, and Frequency Control* **2018**, *65*, 2167–2175.
- (53) Gong, S.; Piazza, G. Design and Analysis of Lithium–Niobate-Based High Electromechanical Coupling RF-MEMS Resonators for Wideband Filtering. *IEEE Transactions on Microwave Theory and Techniques* **2013**, *61*, 403–414.
- (54) Liu, Y.; Cai, Y.; Zhang, Y.; Tovstopyat, A.; Liu, S.; Sun, C. Materials, Design, and Characteristics of Bulk Acoustic Wave Resonator: A Review. *Micromachines* **2020**, *11*.
- (55) Yokoyama, T.; Iwazaki, Y.; Onda, Y.; Nishihara, T.; Sasajima, Y.; Ueda, M. Highly piezoelectric co-doped AlN thin films for wideband FBAR applications. *IEEE Transactions on Ultrasonics, Ferroelectrics, and Frequency Control* **2015**, *62*, 1007–1015.

- (56) Naumenko, N. F. High-velocity non-attenuated acoustic waves in LiTaO₃/quartz layered substrates for high frequency resonators. *Ultrasonics* **2019**, *95*, 1 – 5.
- (57) Jaeken, J. W.; Cottenier, S. Solving the Christoffel equation: Phase and group velocities. *Comput. Phys. Commun.* **2016**, *207*, 445 – 451.
- (58) Kazan, M.; Moussaed, E.; Nader, R.; Masri, P. Elastic constants of aluminum nitride. *Phys. Status Solidi c* **2007**, *4*, 204–207.